Front. Struct. Civ. Eng. 2023, 17(10): 1535–1553
https://doi.org/10.1007/s11709-023-0003-0

RESEARCH ARTICLE

# Printability and hardening performance of three-dimensionally-printed geopolymer based on lunar regolith simulant for automated construction of lunar infrastructure

**Feng LI[a], Rongrong ZHANG[a], Siqi ZHOU[a*], Xingyi ZHU[b]**

[a] *School of Transportation Science and Engineering, Beihang University, Beijing 100083, China*
[b] *Key Laboratory of Road and Traffic Engineering of Ministry of Education, Tongji University, Shanghai 200092, China*
[*] *Corresponding author. E-mail: zsq47@buaa.edu.cn*



**ABSTRACT** Using an *in situ* lunar regolith as a construction material in combination with 3D printing not only reduces the weight of materials carried from the Earth but also improves the automation of lunar infrastructure construction. This study aims to improve the printability of a geopolymer based on a BH-1 lunar regolith simulant, including the extrudability, open time, and buildability, by controlling the temperature and adding admixtures. Rheological parameters were used to represent printability with different water-to-binder ratios, printing temperatures, and contents of additives. The mechanical properties of the hardening geopolymer with different filling paths and loading directions were tested. The results show that heating the printed filaments with a water-to-binder ratio of 0.32 at 80 °C can adjust the printability without adding any additive, which can reduce the construction cost of lunar infrastructure. The printability of the BH-1 geopolymer can also be improved by adding 0.3% Attagel-50 and 0.5% polypropylene fiber by mass at a temperature of 20 °C to cope with the changeable environmental conditions on the Moon. After curing under a simulated lunar environment, the 72-h flexural and compressive strengths of the geopolymer specimens reach 4.1 and 48.1 MPa, respectively, which are promising considering that the acceleration of gravity on the Moon is 1/6 of that on the Earth.

**KEYWORDS** geopolymer, lunar regolith simulant, 3D printing, rheology, printability

## 1 Introduction

Building a moon base is crucial in guaranteeing the safety of lunar exploration operations and creating research infrastructure for the scientific study of the Moon [1]. Lunar base construction heavily relies on the critical technology of *in situ* resource utilization [2]. Using local materials on the lunar surface as building materials for a lunar base can significantly lower construction costs by reducing the weight of materials that need to be carried when launching a spacecraft from the Earth [3]. Lunar regolith is the most easily obtained *in situ* lunar resource as it has the largest reserves on the Moon. Scientists worldwide have pursued diverse technological approaches, including high-temperature sintering and hardening [4], use of sulfur in lunar regolith to synthesize sulfur concrete [5], and geopolymerization [6] to create construction materials utilizing lunar regolith or similar materials. Of these methods, high-temperature sintering has the disadvantages of high separation requirement and high energy consumption, making it difficult to apply in practice. Sulfur concrete also lacks application prospects owing to its poor tolerance to high temperatures [6] and lack of known mature technology routes for sulfur extraction from lunar regolith.

Geopolymer is composed of polymerized gels containing a three-dimensional (3D) network of silicon–oxygen tetrahedron and aluminum–oxygen tetrahedron, which are

*Article history: Received Nov 10, 2022; Accepted Mar 2, 2023*

produced through the combination of an aluminosilicate precursor and alkali activator [7]. Geopolymer has gained increasing attention in recent years, including for research on lunar base construction, because of its exceptional mechanical strength, thermal insulation, and radiation protection properties [8]. Both the real lunar regolith samples and lunar regolith simulants developed by researchers are mainly composed of $SiO_2$ and $Al_2O_3$ [9], which are essential raw materials for geopolymerization. Montes et al. [10] utilized the JSC-1A simulant to prepare a geopolymer by uniaxial hot pressing. The geopolymer produced exhibited a compressive strength of up to 37 MPa. In addition, it displayed good radiation protection performance. Alexiadis et al. [11] used Martian regolith simulants to prepare geopolymers with a compressive strength of 17.9 MPa using a sodium hydroxide solution as the alkali activator. Therefore, it is reasonable to assume that preparation of lunar building materials using a lunar regolith simulant as a geopolymer precursor has scientific and application prospects in terms of composition substitution and material availability.

3D printing technology is an automated process that involves layer-by-layer stacking of concrete or a geopolymer paste to create building components using a control system and printing extrusion device, which is guided by digital model files [12]. Utilizing 3D printing technology to construct a lunar base using geopolymer made from lunar regolith offers significant benefits such as increased flexibility and automation. This makes it highly suitable for early stage lunar base construction, especially in situations where there is a shortage of manpower. Pilehvar et al. [13] employed urea as a superplasticizer to control a geopolymer consisting of the DNA-1 lunar regolith simulant for the purposes of 3D printing. Cesaretti et al. [14] used the D-shape method, similar to 3D printing, to bond the lunar regolith simulant layer by layer with a saturated solution of magnesium oxide and magnesium chloride hexahydrate as the bonding agent. However, owing to the lack of magnesium in the lunar regolith, all the bonding agents must be carried from the Earth.

Compared with casting, 3D printing has more special requirements on the printability of cementitious materials [15,16], including extrudability [17], buildability [18], and open time [18], which are usually characterized by rheological parameters [19]. When the printability of a cementitious material is unqualified, an admixture can be used to adjust its printability [13]. However, the admixtures used in the previous studies, such as hydroxypropyl methylcellulose [17], nano-attapulgite clay [20], polycarboxylate [21], and fibers [22], are mainly applied to improve the printability of cement mortar [23] and geopolymers whose precursors are earth minerals such as fly ash [24]. The effect of admixtures is not clear in the geopolymer based on a lunar regolith simulant. Furthermore, carrying admixtures from the Earth for *in situ* 3D printing on the Moon adds additional space transportation costs. If a method can be proposed to improve printability without admixtures, the cost of lunar 3D printing is further reduced. According to a previous research conducted by the authors of this article [25], the solidification rate of a geopolymer made of a lunar regolith simulant increases with the increase in temperature. Thus, it is reasonable to assume that the use of a temperature controller can regulate the printability of a geopolymer made of a lunar regolith simulant.

The aim of this study is to explore the potential of temperature adjustment in achieving satisfactory printability for a geopolymer derived from a lunar regolith simulant. Additionally, this study aims to evaluate the efficacy of the two most widely used rheological modifiers, attapulgite and polypropylene (PP) fiber, for 3D printing of inorganic cementing materials. The final goal is to create a geopolymer mixture and develop a 3D printing process using a lunar regolith simulant that can withstand the challenging curing conditions on the lunar surface.

## 2 Materials and methods

### 2.1 Materials

#### 2.1.1 Lunar regolith simulants

BH-1 is a simulant material that closely resembles the Apollo 14 genuine lunar regolith in terms of chemical composition, mineralogy, reflectance spectrum, and microscopic features [25,26]. The chemical composition of the BH-1 lunar regolith simulant is presented in Table 1. The differences in the $SiO_2$ and $Al_2O_3$ contents, which are

**Table 1** Comparison of main element contents in BH-1 simulated lunar soil and Apollo 14 real lunar soil (%)

| element | content | | | |
|---|---|---|---|---|
| | real lunar regolith collected by Apollo 14 | JSC-1 lunar regolith simulant | CAS-1 lunar regolith simulant | BH-1 lunar regolith simulant |
| $SiO_2$ | 48.10 | 47.70 | 49.20 | 43.30 |
| $TiO_2$ | 1.70 | 1.60 | 1.90 | 2.90 |
| $Al_2O_3$ | 17.40 | 15.00 | 15.80 | 16.50 |
| FeO | 10.40 | 10.80 | 11.50 | 16.70 |
| MnO | 0.14 | 0.18 | 0.14 | 0.30 |
| MgO | 9.40 | 9.00 | 8.70 | 3.00 |
| CaO | 10.70 | 10.40 | 7.50 | 8.80 |
| $Na_2O$ | 0.70 | 2.70 | 3.10 | 3.80 |
| $K_2O$ | 0.55 | 0.82 | 1.03 | 3.30 |
| $P_2O_5$ | 0.51 | 0.66 | 0.30 | 0.70 |

most closely related to geopolymerization, between BH-1 and the Apollo 14 lunar regolith sample are less than 5%. It should be noted that the compositional differences between the JSC-1 [27] and CAS-1 [28] lunar regolith simulants and real lunar soil are similar to that of BH-1, as indicated in Table 1. The mineralogical analysis based on X-ray diffraction (XRD) pattern is shown in Fig. 1(a). BH-1 primarily comprises albite-high, andesine, anorthite, and labradorite, which are also the primary minerals found in genuine lunar regolith samples. The reflectance spectra of the real lunar regolith sample [29] and BH-1 are shown in Fig. 1(b), which have high similarity as the lines almost coincide at wavelengths between 400 nm and 900 nm. BH-1 measured using scanning electron microscope (SEM) has a loose and porous micromorphology, showing great similarity with the Apollo lunar regolith sample [29], as shown in Figs. 1(c) and 1(d). The bulk density of BH-1 is 1103 kg·m$^{-3}$.

### 2.1.2 Alkali-activator and rheological modifier

The alkali-activator consists of analytically pure sodium hydroxide (NaOH) and distilled water.

Attagel-50 thixotropic agent and PP fiber were used as rheological modifiers to improve the printability in 3D printing. Attagel-50 thixotropic agent is a type of attapulgite produced by BASF Corporation, Germany. The main composition of Attagel-50 is magnesium aluminosilicate hydrate, with the chemical formula of $3MgO\text{-}1.5Al_2O_3\text{-}8SiO_2\text{-}9H_2O$. The median particle size is 9 μm, and its density is 400 kg·m$^{-3}$. The PP fiber was provided by Shanghai Qichen Chemical Technology Co., Ltd., China. The main performance parameters of the PP fiber are listed in Table 2.

## 2.2 Experimental methods

### 2.2.1 Printability

The 3D printer was manufactured by Zhichuangcheng Technology Co., Ltd., Xiamen, China. The 3D printer is a gantry structure, and the drive motor, stock screw, storage hopper, and extrusion nozzle together constitute the feeding mechanism. The 3D model was modeled using the SolidWorks software and imported into the Simplify3D software for slicing as a G-code file matching 3D printer.

The printability of the geopolymer based on the BH-1 lunar regolith simulant includes three aspects: extrudability, open time, and buildability.

In this study, the extrudability of the material was evaluated using the 3D printer feeding mechanism. The

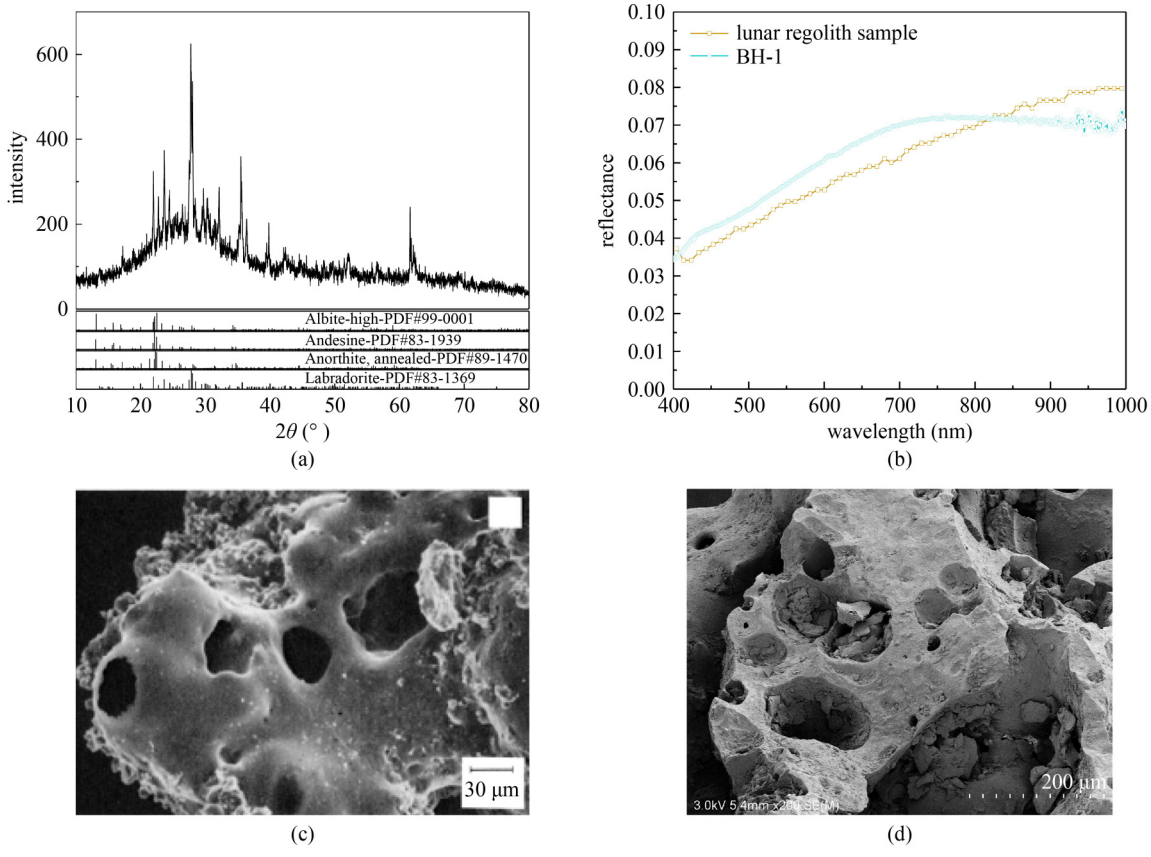


**Fig. 1** Material characteristics of BH-1 lunar regolith simulant: (a) XRD patterns of BH-1; (b) reflectance spectra of BH-1 and real lunar regolith; (c) SEM microscopes of real lunar regolith sample (NASA S87-39605); (d) SEM image of BH-1.

**Table 2** PP fiber performance parameters

| parameter | value |
|---|---|
| length (mm) | 3 |
| diameter (μm) | 32 |
| density (kg·m$^{-3}$) | 910 |
| tensile strength (MPa) | ⩾ 460 |
| Young's modulus (MPa) | ⩾ 3500 |
| ignition point (°C) | 580 |

fresh geopolymer pastes were filled into the storage hopper and screwed to form a 2000-mm-long filament [30]. The results were evaluated in terms of "extrudable," "not extrudable," and "not screwable" [31]. The open time is the duration during which the material can be extruded after the completion of mixing.

Buildability refers to the capacity of the geopolymer to maintain its shape during the vertical stacking of the filament layers [15]. In previous studies, the buildability was mostly evaluated by printing structures comprising a certain number of layers and evaluating the point at which they collapse based on their vertical height [32], or by printing structures with a certain number of layers to measure the collapse size of vertical height [17,30]. In this study, the "vase mode" of the 3D printer was used to print a ring structure with a bottom surface of 100 mm × 100 mm, as shown in Fig. 2. That is, the cube shell was printed in a single-layer spiral manner, and the number of layers printed when the specimen collapsed was recorded. Each experimental group was subjected to three parallel tests, and the results were recorded based on the average number of printed layers.

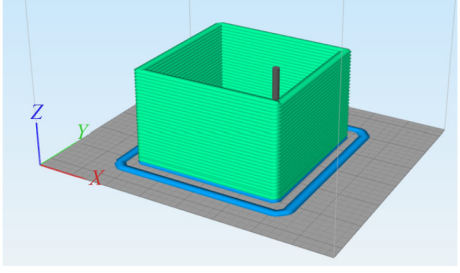


**Fig. 2** Slice model for buildability test.

### 2.2.2 Rheological properties

A rotational rheometer (MCR 702 MultiDrive, Anton Paar, Austria) was used to measure the rheological properties of the BH-1 geopolymer, including static yield stress ($\tau_s$), dynamic yield stress, and plastic viscosity. To store the samples during the measurements, a fixture called the FlexibleCupHolder system was used, which could accommodate a standard measuring cup with a diameter of 42 mm. The measuring rotor of an ST30-4V-40 cylinder spindle, which measures 30 mm in diameter and 40 mm in length, was employed in the testing.

The test method of $\tau_s$ in this study is as follows: the BH-1 geopolymer paste was pre-sheared for 20 s at a shear rate of 0.01 s$^{-1}$. Subsequently, a rotation test was performed at a shear rate of 0.1 s$^{-1}$ for 60 s. The variation in the shear stress $\tau$ with time was recorded, and the peak stress was denoted as $\tau_s$. The $\tau_s$ value is indicative of the least amount of stress necessary to initiate flow in the fluid and indicates the printability of the materials utilized in 3D printing. A higher $\tau_s$ of the paste corresponds to a higher buildability.

The testing principle is shown in Fig. 3. A linearly increasing strain was applied to the BH-1 geopolymer gel. That is, the specimen was sheared at a constant shear rate. Before the critical strain was reached, the shear stress showed a time-dependent linear increase as the elastic element of the material was stretched in the shear field. When the paste was at rest, a flocculent structure was formed owing to the interlocking between the solid particles of BH-1, which acted as the linear element in Fig. 3. When the elastic element approached its critical strain, the structure began to break, viscoelastic deformation occurred, and the stress growth rate slowed down. Eventually the geopolymer gel was completely destroyed and started to flow. At this time, the shear stress reached the peak value, $\tau_s$.

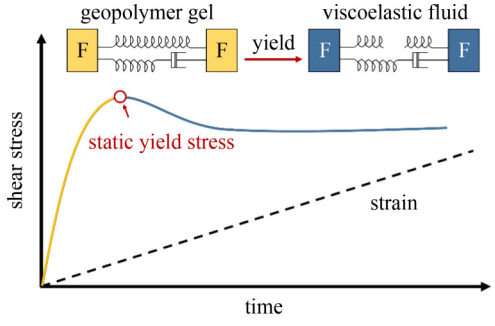


**Fig. 3** Testing principle of static yield stress.

The test procedure for dynamic yield stress and plastic viscosity was conducted according to ASTM standard D2196 [33]. The paste was pre-sheared for 20 s when the shear rate was 0.01 s$^{-1}$, and the shear rate was increased linearly from 0 to 100 s$^{-1}$ within 100 s; this is called the increasing flow curve. Subsequently, the shear rate was reduced linearly from 100 s$^{-1}$ to 0 within 100 s; this is called the decreasing flow curve. The variation in apparent viscosity in the descending curve with shear rate was recorded. The test results were fitted using the Bingham model as shown in Eq. (1):

$$\tau = \tau_0 + \mu\dot{\gamma}, \tag{1}$$

where $\tau$ is the shear stress, $\tau_0$ is the dynamic yield stress [34], $\mu$ is the plastic viscosity, and $\dot{\gamma}$ is the shear rate.

### 2.2.3 Mix proportions and preparation of geopolymer based on BH-1

Two methods were adopted to improve the BH-1 geopolymer printability.

The first method is printing temperature adjustment. The advantage of this method is that additional admixtures need not be carried from the Earth. The disadvantage is that the 3D printing equipment needs to be well sealed to ensure accurate temperature control.

The hardening and rheological time-varying properties of BH-1 geopolymers have high temperature sensitivity [25]. High temperature can accelerate the fluid–solid transformation rate of geopolymer paste, resulting in an increase in viscosity. Upon using this feature and a 3D printing device with temperature adjustment function, the paste theoretically hardens slowly in the storage hopper under a relatively low temperature while it is subjected to the anti-flocculation effect of the screw agitation, which can maintain the fluidity and improve the extrudability. As the extruded filament is deposited onto the print bed, the 3D printing chamber applies heat to the filaments, which quickens the hardening process and enhances the buildability.

The second method involves using the Attagel-50 thixotropic agent and PP fiber as rheological modifiers. We investigate how the water-to-binder ratio (*W*/*B* ratio) and amounts of the two rheological modifiers (Attagel-50 thixotropic agent and PP fiber) impact the rheological characteristics of the BH-1 geopolymer; Table 3 displays the mixing proportions. The procedure for producing the geopolymer pastes utilizing BH-1 involved mixing the BH-1 regolith simulant with an alkali activator solution using a mortar mixer.

**Table 3** Mix design to study the effect of different admixture contents on rheological properties

| series | water-to-binder ratio | mass ratio of PP fiber to BH-1 | mass ratio of Attagel-50 to BH-1 |
|---|---|---|---|
| W30 | 0.30 | 0 | 0 |
| W32 | 0.32 | 0 | 0 |
| PP3_1.0% | 0.32 | 1.0% | 0 |
| PP3_1.5% | 0.32 | 1.5% | 0 |
| PP3_2.0% | 0.32 | 2.0% | 0 |
| ATT0.3% | 0.32 | 0 | 0.3% |
| ATT0.5% | 0.32 | 0 | 0.5% |
| ATT1.0% | 0.32 | 0 | 1.0% |

To elucidate the impact of different printing temperatures on the rheological properties of the BH-1 geopolymer and to determine the appropriate *W*/*B* ratio and printing temperature, experiments were conducted, as outlined in Table 4. The mixing step and rheological test were the same as mentioned above. Five samples were taken from the pot immediately after the paste mixing was completed. The rheological properties of the first sample were tested immediately after taking it out according to the method described in Subsubsection 2.2.3, which was recorded as 0 min. The other four samples were cured at 40, 60, and 80 °C, respectively, with a rheometer temperature control device (CTD 180). The rheological tests were performed at 10, 20, 30, and 40 min after starting to cure at each temperature.

**Table 4** Mixing scheme for studying the impact of different water-to-binder ratios and printing temperatures on rheological properties

| test group | BH-1 (g) | NaOH (g) | water (g) | printing temperature (°C) |
|---|---|---|---|---|
| W30T40 | 1000 | 90 | 300 | 40 |
| W30T60 | 1000 | 90 | 300 | 60 |
| W30T80 | 1000 | 90 | 300 | 80 |
| W32T40 | 1000 | 90 | 320 | 40 |
| W32T60 | 1000 | 90 | 320 | 60 |
| W32T80 | 1000 | 90 | 320 | 80 |

The determination of printability and establishment of its relationship with the rheological parameters are shown in Fig. 4 aimed at enhancing printability.

### 2.2.4 Mechanical strength

The mechanical characteristics of cured 3D-printed samples are influenced not only by the mixing plan but also by the filling path and loading direction during the printing process.

Five types of filling path in the Slicer 3D software, including wiggle, fast honeycomb, rectilinear with routing angle of 30°/−30°, rectilinear with routing angle of 45°/−45°, and rectilinear with routing angle of 90°/−90°, were set to print specimens of size 40 mm × 40 mm × 160 mm based on the BH-1 geopolymer, which were then cured under simulant lunar temperature and vacuum conditions for 72 h according to a previous study [35]. The test procedure of mechanical properties was in accordance with the specification of GBT-17671-2020 [36]. Loading was applied along the *Z* direction.

The 3D printed specimens showed obvious anisotropy [37,38]. The layer-by-layer stacking may form a weak interlayer interface, which further introduces the problem of mechanical anisotropy. As shown in Fig. 5, specimens of size 40 mm × 40 mm × 160 mm were printed in the rectilinear with routing angle of 45°/−45° filling path with an optimized 3D printing formula, and the temperature was determined by the rheological analysis. The curing conditions and mechanical property test were the same as above. The flexural strength was tested by loading in the *Y* and *Z* directions, denoted as F-*Y* and F-*Z*, respectively. A cube of size 40 mm × 40 mm × 40 mm was cut from the specimen for the compressive strength

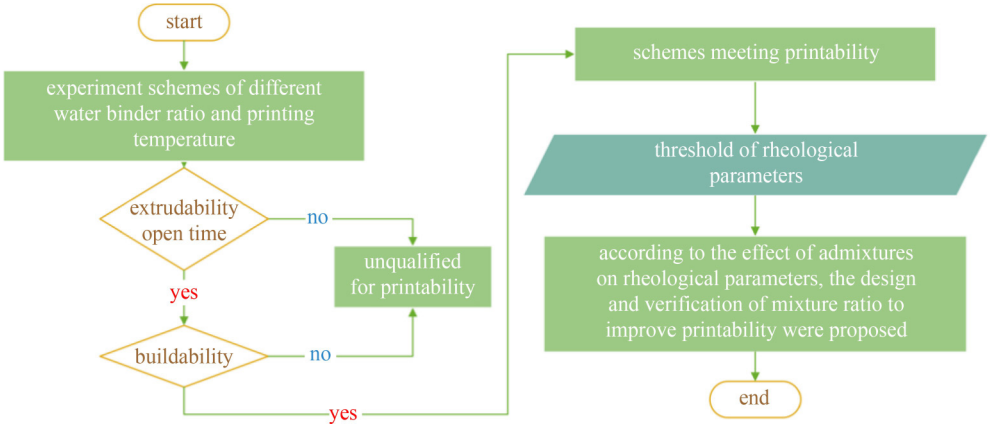


**Fig. 4** Establishment of correlation between printability and rheological parameters and printability optimization.

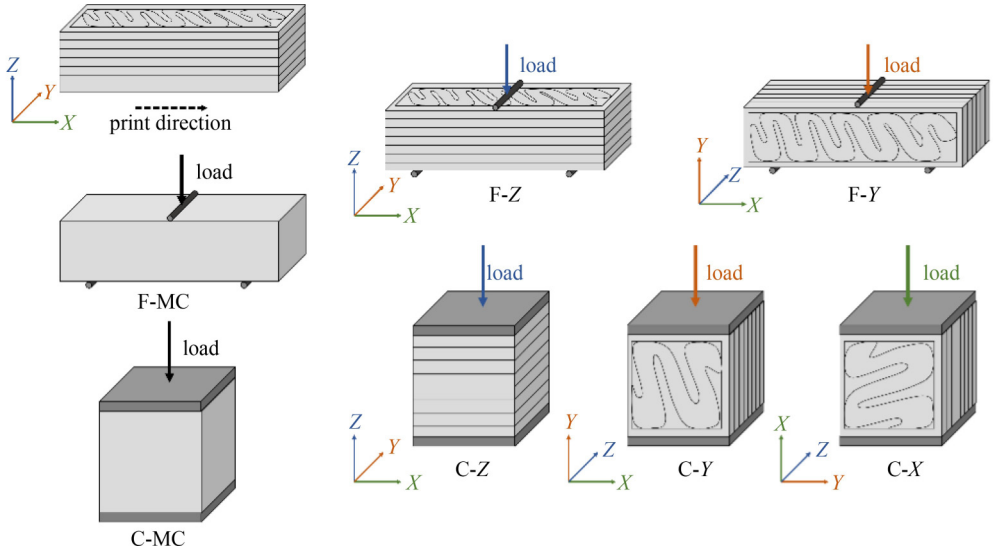


**Fig. 5** Loading method of 3D printing hardened specimens.

test, which was then loaded in three directions, *X*, *Y*, and *Z*, denoted as C-*X*, C-*Y*, and C-*Z*, respectively. The experiments were conducted thrice in each direction, and the resulting mean value was considered the outcome. Additionally, cast specimens were cured under identical conditions, and their flexural (F-MC) and compressive strengths (C-MC) were measured for comparison purposes.

## 3 Results and discussion

### 3.1 Effect of different factors on rheological parameters

#### 3.1.1 Water-to-binder ratio

The rheological parameters of the BH-1 geopolymer with different water contents are presented in Fig. 6 and Table 5. It can be seen from Fig. 6(a) that with the continuous increase in strain, the stress of all plots show a linear growth at first, then a decrease in growth rate, and a gentle decline after reaching the peak value. The $\tau_s$ value decreases with the increase in the water content, as indicated in Table 5. This is because with the decrease in the volume fraction of solid in the paste, the interlocking between the solid particles and flocculent structure is weakened.

Bingham's model was found to be applicable to geopolymer pastes with various *W*/*B* ratios, as depicted in Fig. 6(b). With the increase in the *W*/*B* ratio, both $\tau_0$ and $\mu$ showed a downward trend. $\tau_0$ refers to the shear stress required for a stable flow of paste in shear equilibrium state. When the *W*/*B* ratio increases, the solid volume fraction of the paste decreases and $\tau_0$ also decreased. Because the number of flocculated structures in shear equilibrium is less than that in the initial flow stage, $\tau_0$ is smaller than $\tau_s$. $\mu$ represents the internal friction between particles in the flow process. As $\mu$ increases, the shear stress needed to achieve a similar flow rate also increases. An increase in the *W*/*B* ratio leads to an increase in the free water content, a decrease in the internal friction, and a decrease in $\mu$.

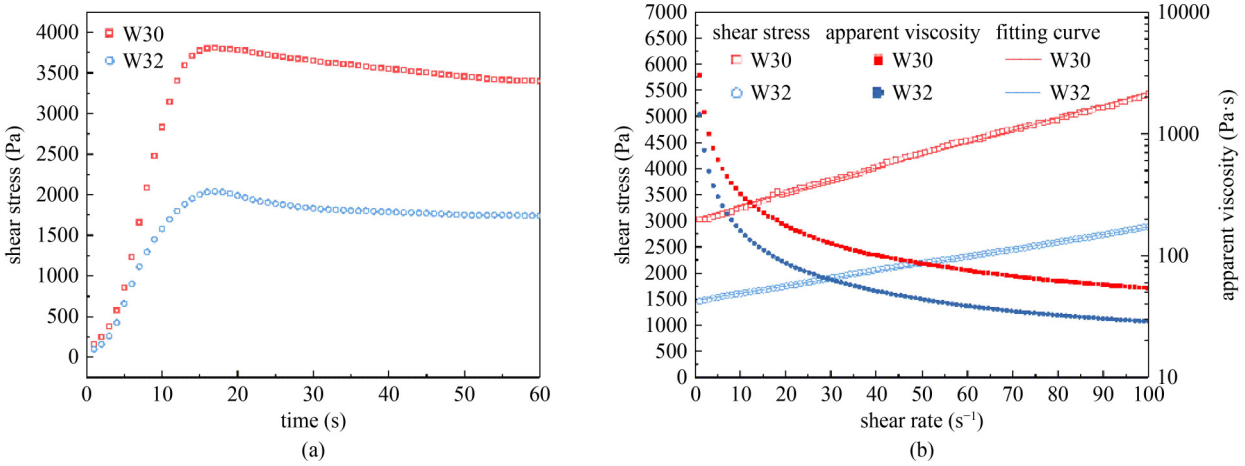


**Fig. 6** Effect of different *W*/*B* ratios on rheological parameters: (a) static yield stress test curve; (b) descending flow curve and apparent viscosity curve.

**Table 5** Rheological parameters of experimental groups with different *W*/*B* ratios

| rheological parameter | W30 | W32 |
|---|---|---|
| static yield stress (Pa) | 3803.7 | 2039.8 |
| dynamic yield stress (Pa) | 3040.98 | 1471.53 |
| plastic viscosity (Pa·s) | 24.15 | 14.08 |

The quantitative changes in the rheological parameters describe the conflict between extrudability and buildability of the 3D printing paste. When the *W*/*B* ratio is relatively large, the $\tau_0$ and $\mu$ values of the slurry are low, which facilitates pump transport and nozzle extrusion, thus benefitting the extrusion process. However, the decrease in $\tau_s$ with an increase in the *W*/*B* ratio is detrimental to buildability.

### 3.1.2 Polypropylene fiber contents

The rheological parameters of the BH-1 geopolymer with different PP fiber contents are shown in Fig. 7. With the increase in the fiber content, $\tau_s$ of the paste increased. Moreover, when the PP fiber content was 1.0% and 1.5%, $\tau_s$ increased by 19.1% and 30.6%, respectively. When the PP fiber content was 2.0%, $\tau_s$ increased by 72.9%, and its growth range was significantly larger. According to the formation mechanism of $\tau_s$, the gel formed by geopolymerization in the pastes served as an elastic unit. The PP fiber had a bridging effect, which could delay the rupture of the gel under shear. When the mixing amount was higher than a critical value, lap would occurred between the fibers, forming a network structure [39] and leading to an abrupt change in $\tau_s$.

When the fiber content was 1.0%, $\tau_0$ decreased slightly compared with that in the W32 group. When the PP fiber content was increased to 1.5% and 2%, $\tau_0$ increased with the increase in the fiber content. The $\mu$ value increased with the increase in the fiber content. As the second dispersing phase in the paste, the fiber increased the volume fraction of solids, resulting in the increase in $\tau_0$ and $\mu$. The interlocking and collision between PP fibers and BH-1 particles also increased the $\tau_0$ and $\mu$ values.

### 3.1.3 Attagel-50 contents

Figure 8 presents the rheological parameters of the BH-1 geopolymer with varying amounts of Attagel-50. When the content of Attagel-50 was 0.3%, 0.5%, and 1%,

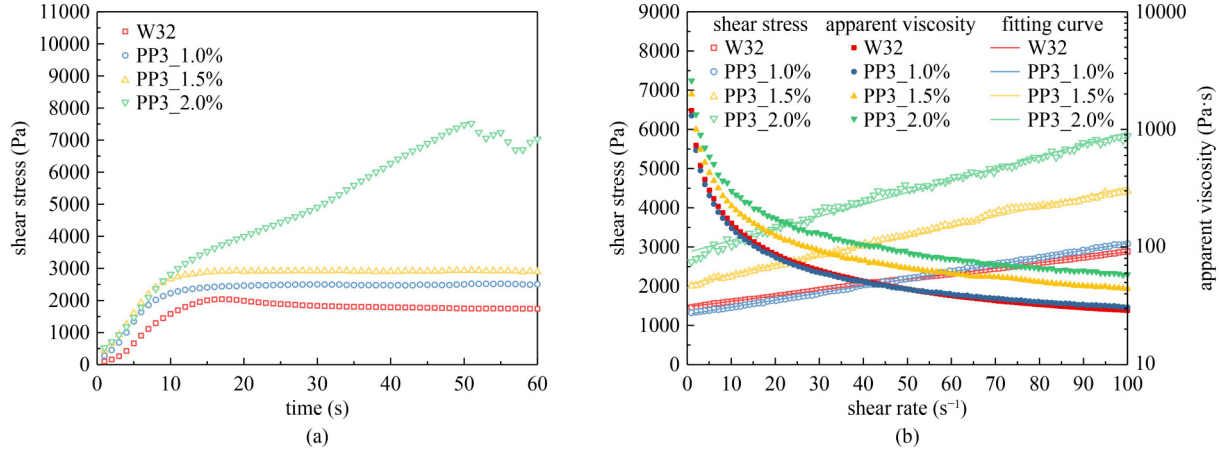

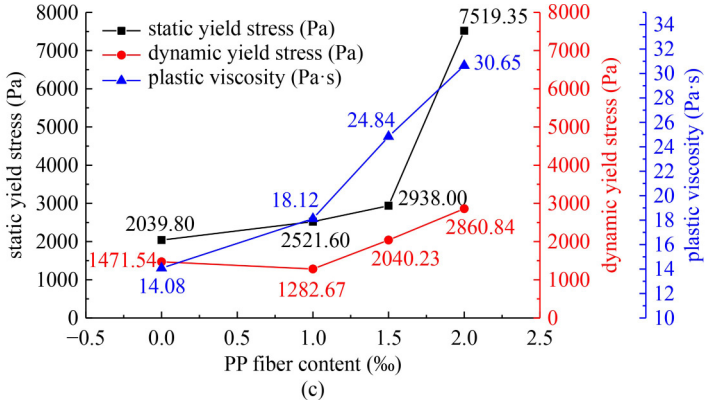


**Fig. 7** Effect of different PP fiber contents on rheological parameters: (a) static yield stress test curve; (b) descending flow curve and apparent viscosity curve; (c) rheological parameters.

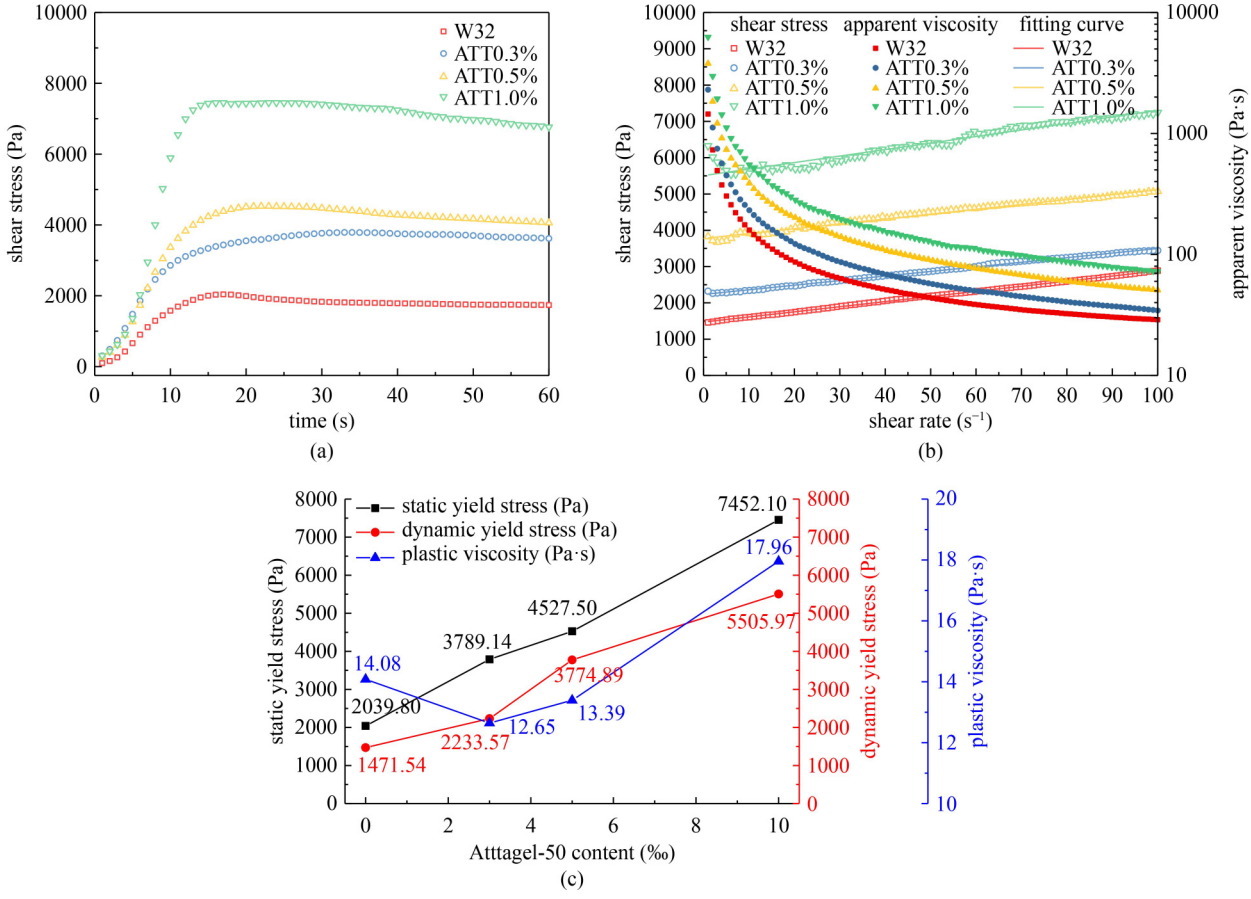


**Fig. 8** Effect of different Attagel-50 contents on rheological parameters: (a) static yield stress test curve; (b) descending flow curve and apparent viscosity curve; (c) rheological parameters.

$\tau_s$ was 1.85, 2.09, and 3.65 times that of the W32 group, and $\tau_0$ was 1.52, 2.57, and 3.74 times that of the W32 group, respectively. Both of them show an increase with the increase in Attagel-50 content. Further, $\mu$ was 0.89, 0.95, and 3.74 times, respectively, that of the W32 group. When the mixing amount was 0.3% and 0.5%, the increase in $\tau_s$ benefited the anti-deformation ability of the 3D-printed structure and the improvement in buildability. The decrease in $\mu$ is beneficial to reduce the residue of paste in the storage hopper. On the contrary, it is inevitable that the concomitant increase in $\tau_0$ will lead to a decrease in extrudability.

Table 6 presents a comparison of the rheological parameters between the experimental group W30 with a *W*/*B* ratio of 0.30 and the experimental group ATT0.3% with a *W*/*B* ratio of 0.32 and Attagel-50 content of 0.3%. It can be observed that value of $\tau_s$ of the two groups is similar, but the $\tau_0$ and $\mu$ values of ATT0.3% are less than

**Table 6** Comparison of rheological parameters between W30 and ATT0.3%

| rheological parameter | ATT0.3% | numerical comparison | W30 |
|---|---|---|---|
| static yield stress (Pa) | 3789.14 | ≈ | 3803.70 |
| dynamic yield stress (Pa) | 2233.57 | < | 3040.98 |
| plastic viscosity (Pa·s) | 12.65 | < | 24.15 |

those of W30. This suggests that on the premise of similar buildability, the extrudability of ATT0.3% is theoretically higher than that of W30.

### 3.1.4 Temperature

The test results of $\tau_s$ with time at different *W*/*B* ratios and temperatures are shown in Figs. 9 and 10, respectively.

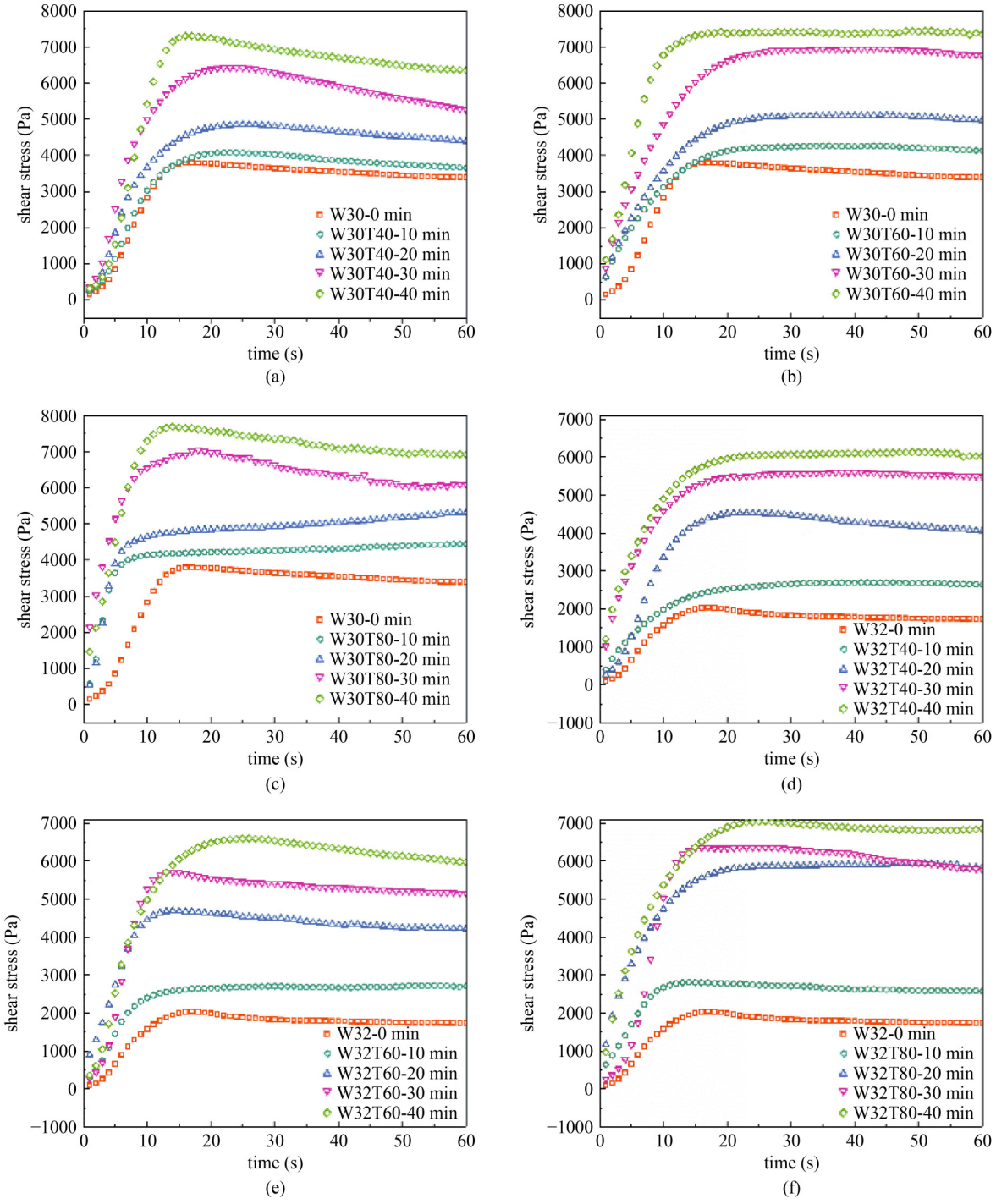


**Fig. 9** Test curves of static yield stress at different *W*/*B* ratios and temperatures: (a) W30T40; (b) W30T60; (c) W30T80; (d) W32T40; (e) W32T60; (f) W32T80.

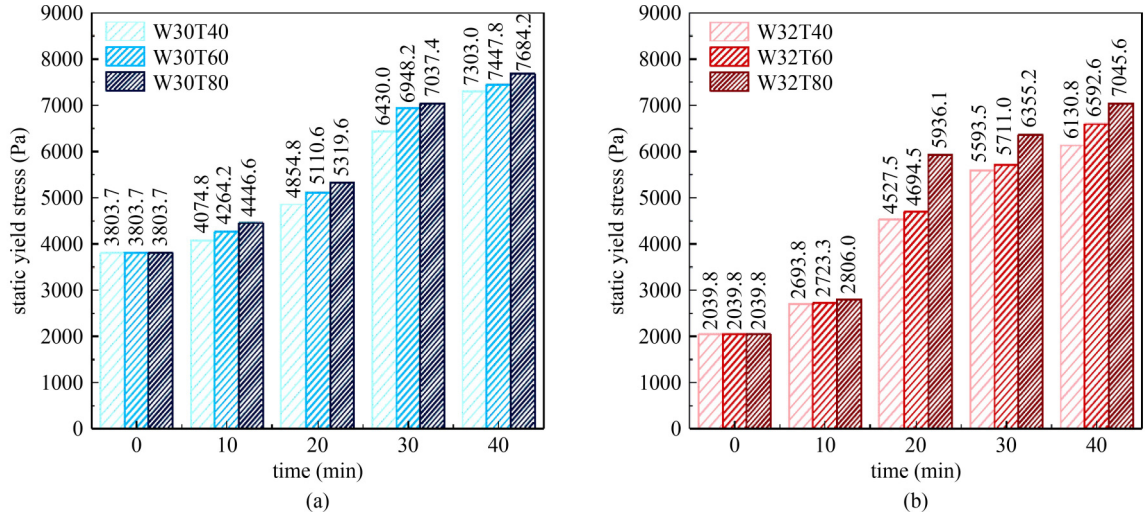


**Fig. 10** Fluctuations in static yield stress over time under different *W*/*B* ratios and temperatures: (a) W30; (b) W32.

The $\tau_s$ value of BH-1 pastes gradually increases with time. The higher the temperature, the faster the growth rate. The rationale is as follows. The intramolecular interactions within the geopolymer paste and coagulation arrangement engendered by the geopolymerization collectively constitute the pliant module. The moisture in the geopolymer paste was vaporized and depleted via geopolymerization over time, diminishing the quantity of free moisture in the paste and intensifying the intermolecular bonding between particles, which brought about an escalation in $\tau_s$.

$\tau_s$ is closely related to the buildability of the 3D printing process [40]. The paste with an increased static output has a higher capability to endure distortion from its own weight and the weight of the top printing layer. By capitalizing on the rapid augmentation of $\tau_s$ as temperature increases, the underlying print structure can be heated to amplify its constructability.

The decreasing flow curves of the BH-1 geopolymer with different *W*/*B* ratios at different temperatures are shown in Fig. 11. The fitting results of $\tau_0$ and $\mu$ are shown in Fig. 12. $\tau_0$ and $\mu$ are related to the free water content in the geopolymer paste and coagulation of particles [41]. At the same temperature and setting time, it can be observed that the $\tau_0$ and $\mu$ values of the BH-1 geopolymer decrease with the increase in the *W*/*B* ratio. With an increase in the *W*/*B* ratio, there was a corresponding decrease in the volume fraction of the solid particles present in the slurry, causing a reduction in internal friction during the flow of the paste. This was evidenced by a decline in both $\tau_0$ and $\mu$.

The $\tau_0$ and $\mu$ values increased with time, which occurred because the free water in the BH-1 pastes was consumed by geopolymerization, and as a consequence, the independent lunar regolith simulant particles formed a gel structure with a strong binding force. The shear stress caused the destruction of the chemical binding force to maintain the flow.

When the *W*/*B* ratio was the same, $\tau_0$ and $\mu$ increased faster with time as the temperature increased. The higher the temperature, the faster the geopolymerization, which resulted in the accelerated growth of $\tau_0$ and $\mu$.

According to Figs. 10 and 12, the variation trends of $\tau_s$, $\tau_0$, and $\mu$ in all the groups increased with time. Long et al. [42] and Liu et al. [17] have observed comparable patterns in the evolution of rheological properties over time. Given that no supplementary components were added after the mixing process, any deviations in the rheological properties were ascribed to differences in the hydration process, which were influenced by temperature.

### 3.2 Effect of different water-to-binder ratio and temperature on printability

#### 3.2.1 Extrudability, open time, and their correlation with rheological parameters

The results of the extrudability test are shown in Fig. 13. When the *W*/*B* ratio was 0.30 at the printing temperature of 40 °C, the open time was 20 min. When the printing temperature was 60 and 80 °C, the open time was less than 10 min. The increase in temperature accelerated the hardening of the geopolymer paste, resulting in the accelerated increase in $\tau_0$ and $\mu$. When the shear stress of the screw remained unchanged, the paste flow rate slowed down and the extrusion flow rate decreased, which eventually led to an extrusion rate less than the *X*/*Y* plane moving speed of the nozzle, showing that the printing strip was broken and could not be extruded continuously. With the further solidification of the paste, the shear of the screw on the material could not make the material flow, that is, the shear force of the screw could not overcome $\tau_s$ of the paste. The extrudability was further attenuated.

When the *W*/*B* ratio was 0.32 at the printing temperatures of 40, 60, and 80 °C, the open time of the

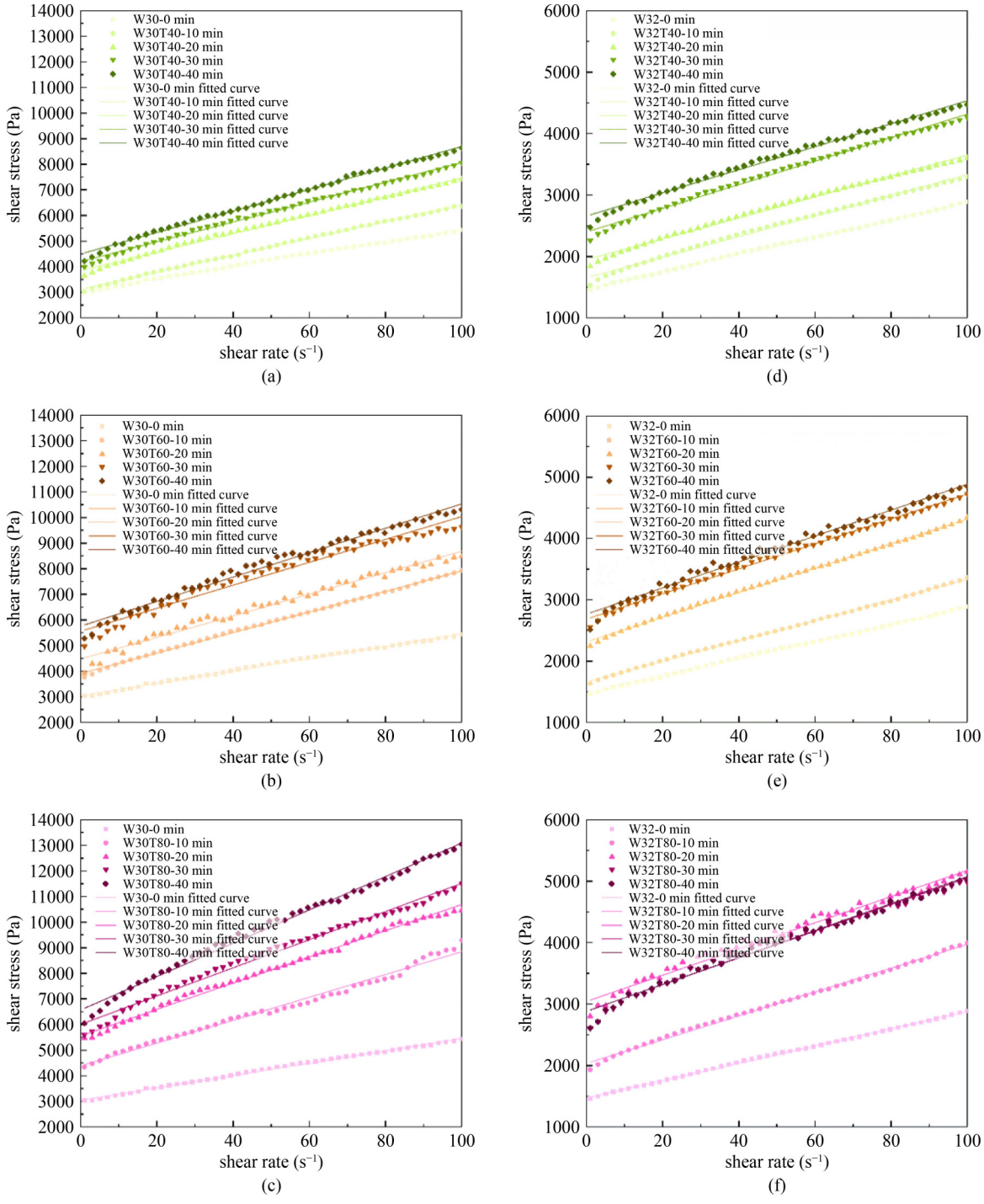


**Fig. 11** Descending curve and Bingham model fitting: (a) W30T40; (b) W30T60; (c) W30T80; (d) W32T40; (e) W32T60; (f) W32T80.

material was 40, 30, and 20 min, respectively. It can be observed that at the same printing temperature, the open time increases with the increase in the *W*/*B* ratio. In addition, under the same *W*/*B* ratio, the higher the printing temperature, the shorter the open time. This occurred because the high temperature accelerated the flocculation of the paste and the decay rate of the material fluidity increased.

To determine the upper and lower limits of extrudability, test groups with *W*/*B* ratios of 0.28 and 0.32 were supplemented. When the *W*/*B* ratio was 0.28, the extrudability test could not be completed at the three temperatures. The paste was blocked at the extrusion nozzle. With the accumulation of paste, the resistance to screw rotation increased, finally leading to fracture. As shown in Fig. 14(a), as the increase in the water content reduced the volume proportion of solid particles in the paste, the additional free water content slowed the

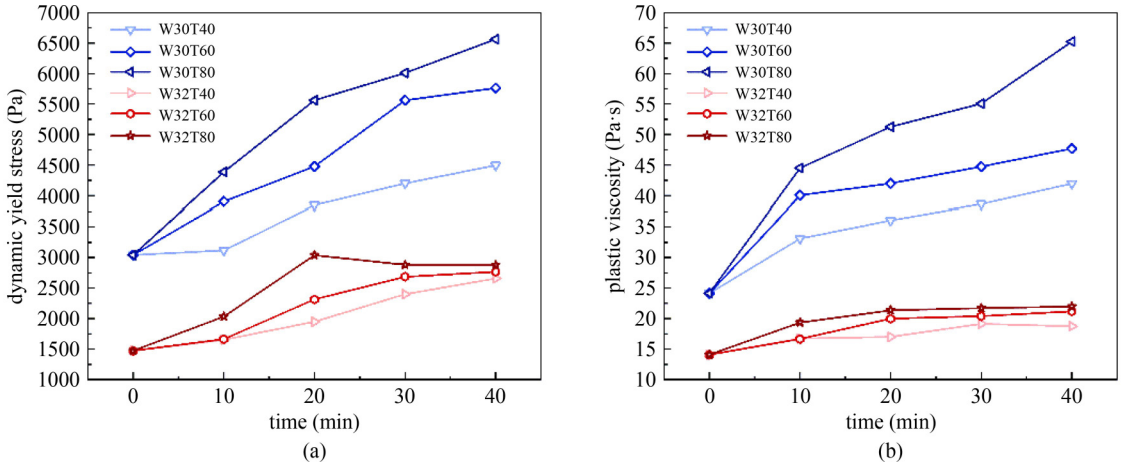


**Fig. 12** Variation in fitting parameters of the Bingham model at different temperatures with time: (a) variation in dynamic yield stress with time; (b) variation in plastic viscosity with time.

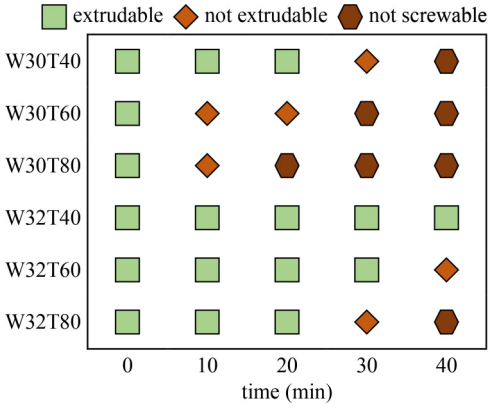


**Fig. 13** Extrudability test results.

geopolymerization rate and attenuation of extrudability. When the *W*/*B* ratio was 0.34, the BH-1 paste flowed excessively, as shown in Fig. 14(b). The printed paste could not form the strip stack structure. The filaments printed by layers were all fused.

### 3.2.2 Correlation between extrudability and rheological parameters

The $\tau_0$ and $\mu$ values of the BH-1 paste at different *W*/*B* ratios and temperatures described in Subsubsection 3.1.4 were plotted in plane coordinates, as shown in Fig. 15. The legend with red circles indicates that the paste is extrudable, while the legend with black blocks indicates

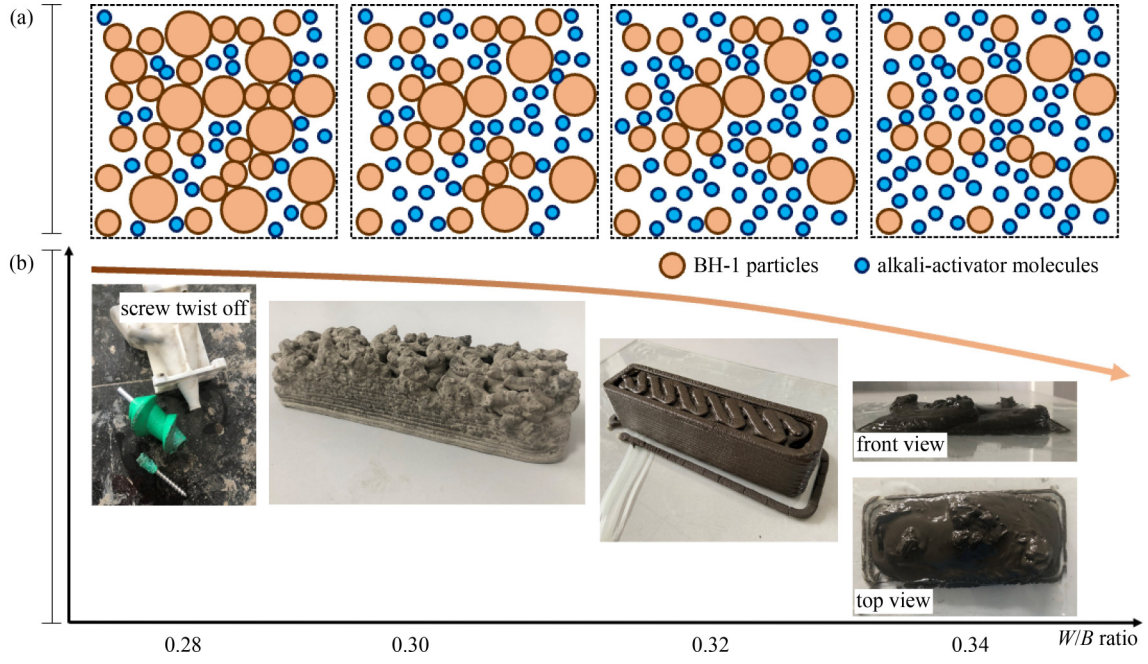


**Fig. 14** Typical stacking form of BH-1 paste with different *W*/*B* ratios and the corresponding diagram of particle packing states: (a) particle packing state; (b) solid volume fraction.

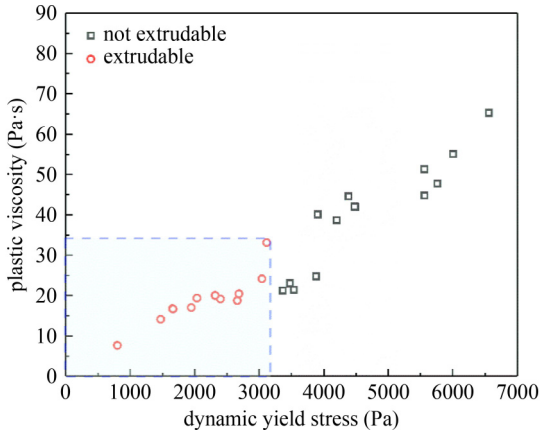


**Fig. 15** Relationship between extrudability and rheological parameters fitted by Bingham model.

that the paste is not extrudable. It can be observed that the upper limit of $\tau_0$ and $\mu$ of the pastes that can be extruded are 3116 Pa and 33.08 Pa·s, respectively. The area enclosed by the two upper limits and coordinate axes covers the extrudable data points.

It is worth mentioning that the threshold values for the rheological parameters obtained in this section are only relevant to the printing device utilized in this study. When the extrusion mechanism and printing parameters change, the rheological parameters must be re-determined.

### 3.2.3 Buildability and its correlation with rheological parameters

The extrudability test findings indicated that when the *W*/*B* ratio was 0.34, the paste was incapable of producing stacked molds. When the *W*/*B* ratio was 0.28, the excessively thick paste damaged the screw and blocked the nozzle. When the *W*/*B* ratio was 0.30, the paste open time was over 20 min only when the printing temperature was 40 °C. When the *W*/*B* ratio was 0.32, the open time of all the test groups exceeded 20 min. Considering that the printing process is time consuming, the buildability test can only be completed if the open time is longer than 20 min. Therefore, four experimental groups, including W30T40, W32T40, W32T60, and W32T80, were finally selected to conduct stacking height and 3D scanning tests to evaluate the buildability.

Figures 16(a) and 16(b) show the typical process of the buildability test. When the limit number of layers was reached, the annular thin wall paste collapsed. The numbers of stacked layers of W30T40, W32T40, W32T60, and W32T80 were 7, 16, 24, and 33, respectively, as shown in Fig. 16(c).

In conclusion, when the *W*/*B* ratio was 0.32, the $\tau_0$ and $\mu$ values of the material were small, which met the requirements of extrudability and open time. At the same time, setting the printing temperature as 80 °C can promote the hardening speed of the lower-layer printed materials, increasing stacking height. Thus, the test group of W32T80 can achieve the balance of extrudability, open time, and buildability and acquires a high quality of printability.

### 3.2.4 Correlation between buildability and rheological parameters

The correlation analysis between the buildability and rheological parameters is as follows. The $\tau_s$ value of the paste represents the time effect of shear stress at a low flow rate, which is consistent with the physical process of slow deformation of the lower-layer printed material under the compression of the dead weight and the upper-layer printed material. Therefore, the buildability can be represented by $\tau_s$. When the *W*/*B* ratio is 0.32, the $\tau_s$ value of the freshly mixed paste varies with time at 40, 60, and 80 °C, as shown in Fig. 17. The slope obtained by linear fitting of the data was the growth rate of $\tau_s$ with time at different temperatures, which increased with rising temperature.

According to the buildability test results in Subsubsection 3.2.3, the fitted vertical intercept (2039.8 Pa) and slope (135.6 Pa·min$^{-1}$) of W32T80 were adopted as the lower limit of the initial $\tau_s$ and growth rate of $\tau_s$ of the BH-1 geopolymer to satisfy the buildability. For the

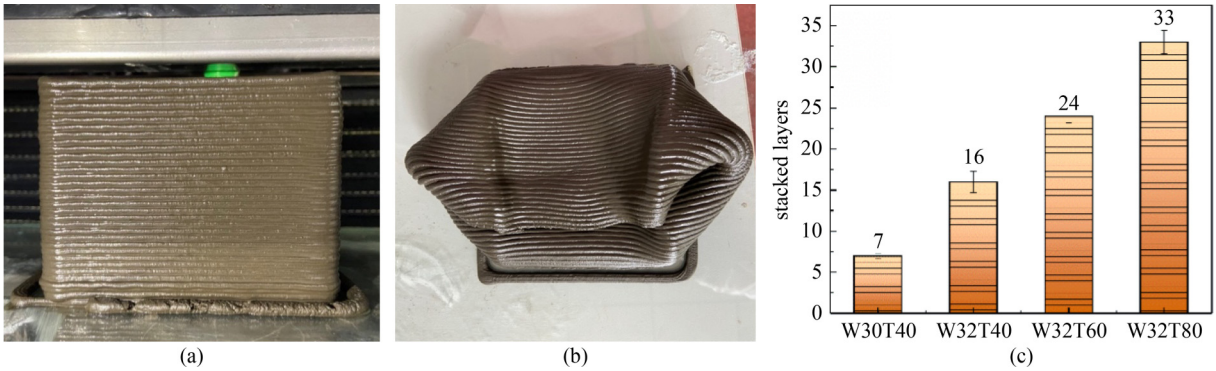


**Fig. 16** Process and results of the buildability test: (a) buildability test process; (b) collapse of the specimen; (c) buildability test results.

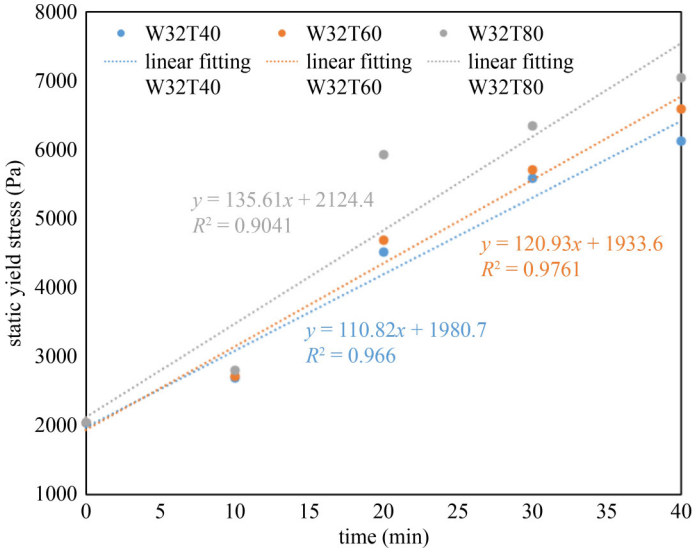


**Fig. 17** Correlation analysis between static yield stress and buildable parameters evaluated by 3D contour scanning.

unheated printing process, the initial $\tau_s$ value of W30T40 (3803.7 Pa) can be used as the lower limit given the hardening rate of the BH-1 geopolymer under room temperature, which can relatively maintain the stability of $\tau_s$.

### 3.3 Optimization of 3D printing formula with admixture

The lunar environment is variable with limited energy supply. When the rheology of the geopolymer paste cannot be controlled using temperature adjustment, the addition of admixtures can be used. From the results presented in Subsection 3.1, it can be inferred that the addition of Attagel-50 to the BH-1 geopolymer paste can enhance the extrudability (reducing $\tau_0$ and $\mu$) without weakening the buildability (similar values of $\tau_s$). The addition of PP fibers improved the $\tau_s$ of the material and enhanced the buildability. Based on the mix design with the best extrudability of 0.32 water–cement ratio, the addition of Attagel-50 with 0.3% mass ratio to the lunar regolith simulant and 0.5% PP fibers was designed to optimize printability, denoted as ADM in Table 7. Specimens with size of 40 mm × 40 mm × 160 mm were printed at 20 °C.

**Table 7** Optimization of mix design of BH-1 geopolymer paste based on rheological parameters

| series | BH-1 (g) | NaOH (g) | water (g) | Attagel-50 (g) | PP fiber (g) | printing temperature (°C) |
|---|---|---|---|---|---|---|
| W32 | 1000 | 90 | 320 | 0 | 0 | 20 |
| ADM | 1000 | 90 | 320 | 3 | 5 | 20 |

The comparison of rheological parameters between W32 and ADM is shown in Fig. 18. It can be observed that after adding Attagel-50 and PP fiber, $\tau_0$ increases from 1471.54 to 2416.20 Pa. $\mu$ decreases slightly from 14.08 to 13.57 Pa·s. The two rheological parameters related to extrudability were within the upper limit obtained in Subsubsection 3.2.2. $\tau_s$ increases from 2039.80 to 4526.90 Pa, which theoretically improves the buildability significantly, meeting the $\tau_s$ lower limit of 3803.7 Pa obtained in Subsubsection 3.2.4.

The extrudability test results are shown in Fig. 19. Owing to the low reactivity of the lunar regolith simulant at 20 °C [25], the rheological characteristic of the paste basically remained unchanged over printing time. The two groups of materials could still be smoothly extruded 40 min after they were well mixed, which reflected the advantage of adjusting the rheological parameters of the BH-1 geopolymer by using admixtures. The reaction inertia at 20 °C could effectively extend the open time. Meanwhile, the admixtures improved the rheological properties to complete the printing process with sufficient time. The printed specimens were then hardened in a high-temperature environment. This improves the efficiency of lunar surface construction.

Drawing from the preceding analysis, it can be deduced that the BH-1 paste with the addition of Attagel-50 and PP fiber as admixtures exhibits favorable extrudability and buildability at a temperature of 20 °C. The open time reaches 40 min.

### 3.4 Hardening properties

#### 3.4.1 Effect of printing path on mechanical properties

Different filling paths of the slicing software and photographs of the printed specimens are shown in Fig. 20. With wiggle, the specimen was filled in a wavy trajectory along the *X* direction. The obvious disadvantage of this filling procedure is that the width of the undulating path along the *Y* direction is related to the nozzle diameter, and the size of the printed pieces along the *Y* direction must be a multiple of the wavy bar width

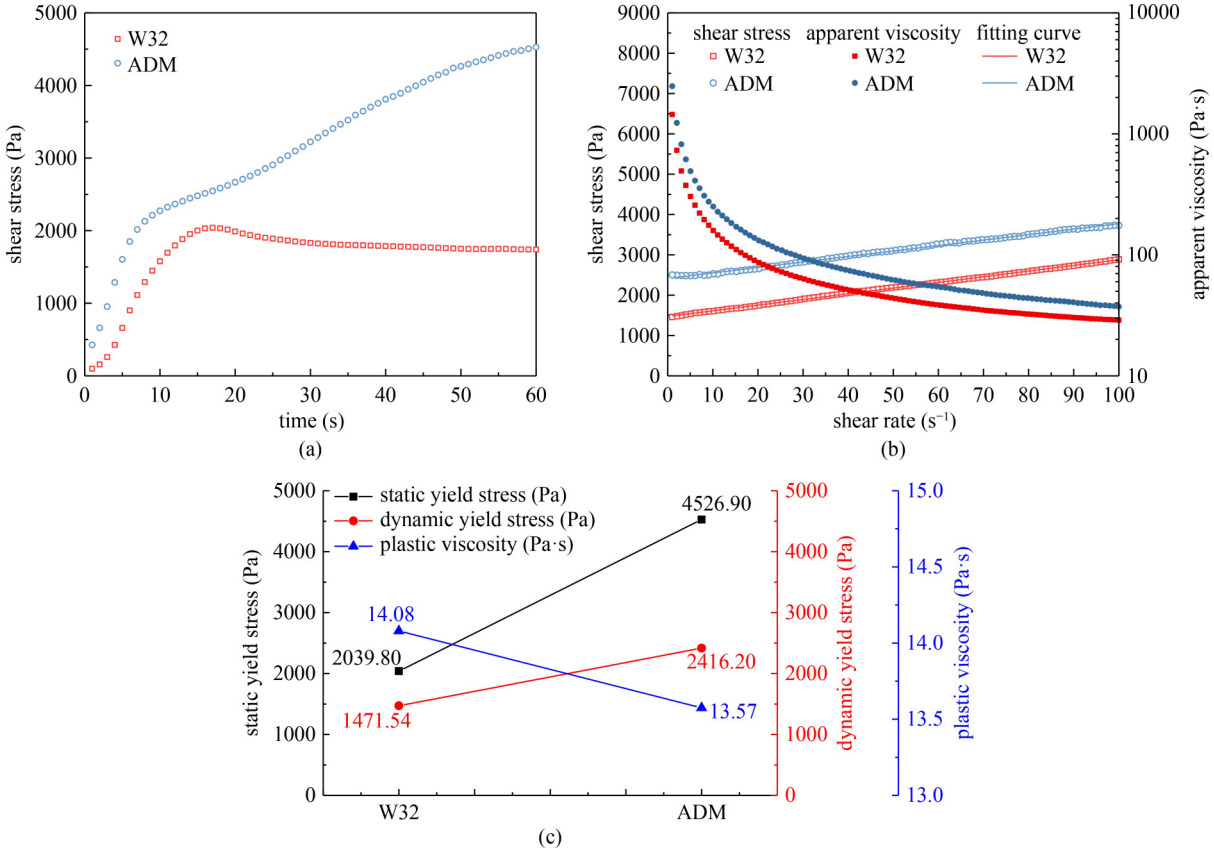


**Fig. 18** Comparison of rheological parameters between W32 and ADM: (a) static yield stress test curve; (b) descending flow curve and apparent viscosity curve; (c) rheological parameters.

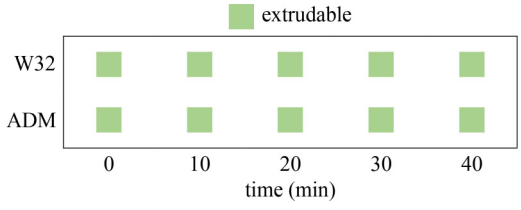


**Fig. 19** Extrudability test results of W32 and ADM.

for a full fill, or filling vacancies appear, as shown in Fig. 20(a), leading to lack of lateral support for the printed ektexine. The ektexine was prone to collapse with the increase in the number of layers.

Fast honeycomb adopts different filling patterns at odd and even layers, and it also suffers from the above problems. There is a lack of filling paste at the corner of the specimen, leading to defects in the corners of the ektexine.

Figures 20(c)–20(e) show rectilinear paths, in which the specimens were filled by a continuous straight S-shaped line. The turning angle near the ektexine can be adjusted by the slicing software. It can be observed that the three specimens printed using rectilinear paths with different turning angles have no obvious defects. Thus, the rectilinear path was determined to be the best among all the selected filling paths. Three specimens of size 40 mm × 40 mm × 160 mm were printed with three different turning angles to study the effect of filling path on the mechanical properties of the hardened BH-1 geopolymer.

The effects of different routing angles on the mechanical strength of the 3D-printed BH-1 geopolymer are shown in Fig. 21. The highest flexural and compressive strength can be achieved when the routing angle is set to 45°/−45°. Meanwhile, if the routing angle is 90°/−90°, the flexural strength of the printed specimen is diminished, as the gap of the U-shaped infill falls in the middle span where stress is maximum, leading to a decrease in the flexural section coefficient. Furthermore, the compressive strength of the printed specimen is at its minimum among the three test groups when the routing angle is 90°/−90°. The flexural and compressive strengths of the printed specimen are almost indistinguishable from those observed when the routing angle is 45°/−45° or 30°/−30°.

### 3.4.2 Effect of loading direction on mechanical properties

Figure 22 illustrates the flexural and compressive strengths of the BH-1 geopolymer specimens fabricated by 3D printing under various loading directions. The specimens exhibited notable anisotropy, indicating

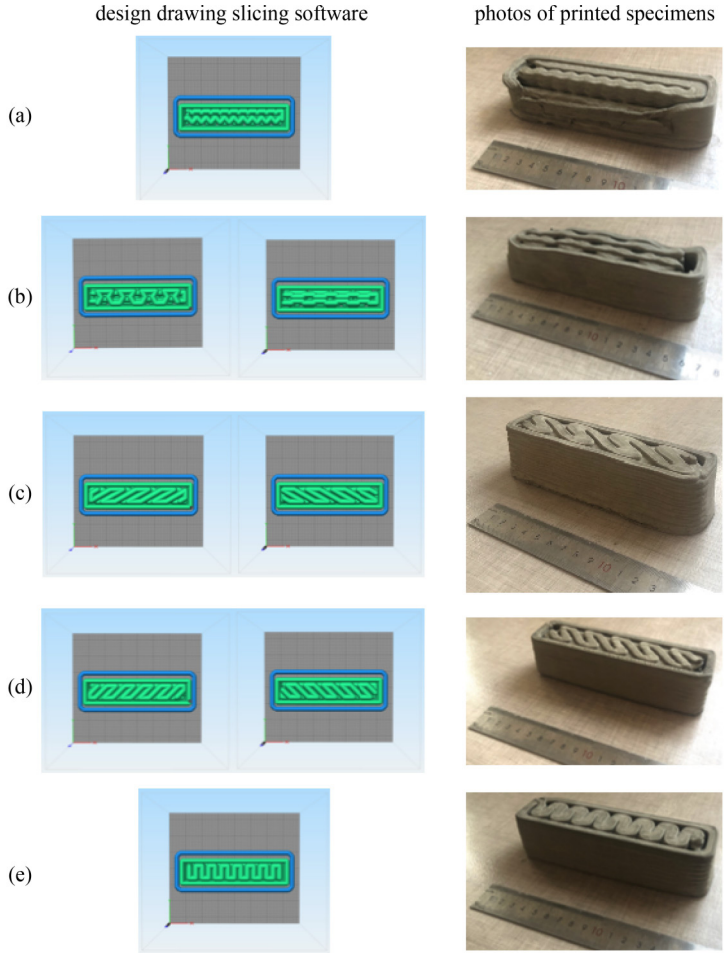


**Fig. 20** Different filling paths of the slicing software and photographs of printed specimens: (a) wiggle; (b) fast honeycomb; (c) rectilinear with routing angle of 30°/−30°; (d) rectilinear with routing angle of 45°/−45°; (e) rectilinear with routing angle of 90°/−90°.

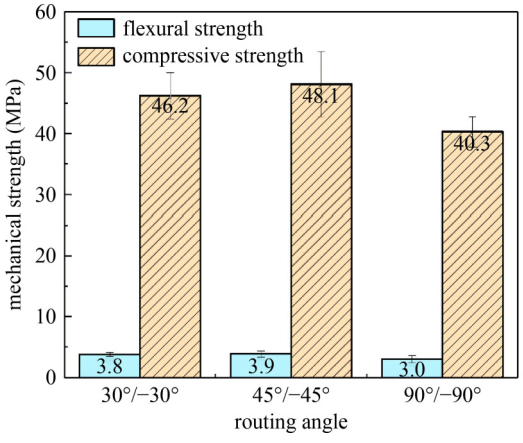


**Fig. 21** Effect of different routing angle on mechanical strength of 3D-printed BH-1 geopolymer.

distinct bearing capacity depending on the loading direction, primarily due to the weak interlayer interface created by the layer-by-layer 3D printing. Furthermore, it is evident that all the mechanical strength values of the 3D-printed specimens are inferior to those of cast specimens.

Nevertheless, it should be noted that the highest flexural and compressive strengths achieved among all the 3D-printed specimens were 4.1 and 48.1 MPa, respectively, which could be considered significant on the Moon, where the gravitational acceleration is only 1/6 of that on the Earth. The decline in compressive strength along the $X$ and $Y$ directions is due to the presence of tensile stress in the fragile interlayer connections, which is in agreement with earlier research findings [43].

## 4 Three-dimensionally-printed special-shaped shelter model with BH-1 geopolymer

Compared with the casting method with formwork, the 3D printing technology has the advantages of flexible modeling, which can print out the structure or component with a special appearance according to the digital 3D model. As shown in Fig. 23, a hollow structure with a curved surface was printed using the BH-1 geopolymer. 3D printing of lunar soil geopolymers can be used to produce bricks for construction in an automated manner

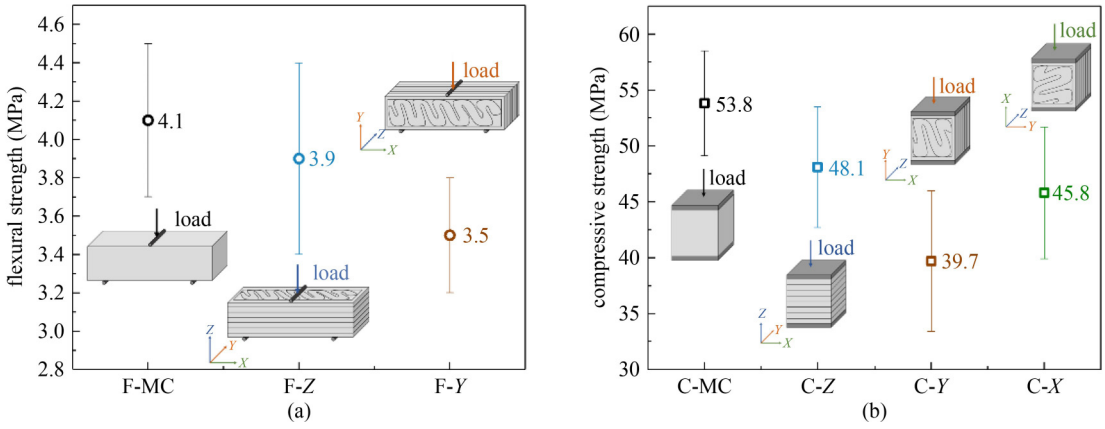


**Fig. 22** Strength properties of 3D-printed specimens subjected to various loading orientations. (a) flexural strength; (b) compressive strength.

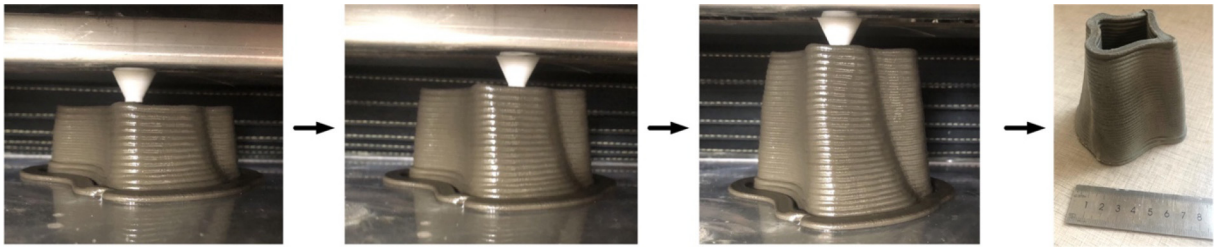

**Fig. 23** Process of printing a special-shaped structure with the BH-1 geopolymer.

or even directly print shelters for astronauts during the construction of a lunar base.

## 5 Conclusions

The following conclusions can be drawn from this study.

1) Heating of the printed filaments can adjust the printability without adding any admixture, which can reduce the construction cost of lunar infrastructure. A high temperature accelerates the growth of $\tau_s$ of a geopolymer based on the BH-1 lunar regolith simulant. Additionally, the paste in the feeding device can maintain good extrudability under low temperature and anti-flocculation of the screw shear. According to the above method, the mixing ratio that met the printability was 0.32 *W*/*B* ratio, and the printing temperature was 80 °C.

2) The printability of the BH-1 geopolymer can be improved by adding additives at the temperature of 20 °C to cope with the changeable environmental conditions on the Moon. The addition of Attagel-50 with 0.3% mass ratio to the BH-1 lunar regolith simulant and 0.5% PP fibers was designed to optimize the printability. Extrudability and buildability of the mixture were qualified with an open time of more than 40 min.

3) Extrudability can be characterized by $\tau_0$ and $\mu$. The upper limits of $\tau_0$ and $\mu$ of the BH-1 geopolymer pastes qualified for extrudability are 3116 Pa and 33.08 Pa·s. Buildability can be characterized by $\tau_s$. The lower limit of the initial $\tau_s$ value and growth rate of $\tau_s$ of the BH-1 geopolymer to satisfy buildability were 2039.8 Pa and 135.6 Pa/min, respectively. For the unheated printing process, an initial $\tau_s$ value of 3803.7 Pa could be used as the lower limit of $\tau_s$.

4) On the basis of good buildability, filling the 3D printing BH-1 geopolymer in a rectilinear path with a routing angle of 45°/−45° provided the best mechanical strength to the curing specimens among all the five types of filling path. The 3D printed specimens had significant anisotropy owing to weak connections between the printed layers. The flexural and compressive strengths reached the maximum in the *Z* direction. After curing under simulated lunar conditions, the 72-h flexural and compressive strengths of the BH-1 geopolymer specimens increased up to 4.1 and 48.1 MPa, respectively, which is promising because the acceleration of gravity on the Moon is 1/6 of that on the Earth.

This study is limited as it uses only one lunar simulant, although its composition is to some extent similar to that of the Apollo samples. Additional simulants must be verified to confirm the results in future work.

**Acknowledgements** This research was supported by the National Natural Science Foundation of China (Grant Nos. 42241128 and 51978029), Key Laboratory of Road and Traffic Engineering of the Ministry of Education, Tongji University (No. K202206), China Postdoctoral Science Foundation (No. 2023M730174), and Young Elite Scientist Sponsorship Program by Beijing Association for Science and Technology (No. BYESS2023418).

**Conflict of Interests** The authors declare that they have no conflict of interest.

## References

1. Wang C, Nie H, Chen J, Lee H P. The design and dynamic analysis of a lunar lander with semi-active control. Acta Astronautica, 2019, 157: 145−156
2. Rapp D. Use of Extraterrestrial Resources for Human Space Missions to Moon or Mars. New York: Springer, 2018, 125–146
3. Qiu Y, Park K. Environment-sensitive hydrogels for drug delivery. Advanced Drug Delivery Reviews, 2012, 64: 49−60
4. Taylor S L, Jakus A E, Koube K D, Ibeh A J, Geisendorfer N R, Shah R N, Dunand D C. Sintering of micro-trusses created by extrusion-3D-printing of lunar regolith inks. Acta Astronautica, 2018, 143: 1−8
5. Toutanji H A, Evans S, Grugel R N. Performance of lunar sulfur concrete in lunar environments. Construction & Building Materials, 2012, 29: 444−448
6. Davis G, Montes C, Eklund S. Preparation of lunar regolith based geopolymer cement under heat and vacuum. Advances in Space Research, 2017, 59(7): 1872−1885
7. Davidovits J. Geopolymers: Inorganic polymeric new materials. Journal of Thermal Analysis and Calorimetry, 1991, 37(8): 1633−1656
8. Xu F, Gu G, Zhang W, Wang H, Huang X, Zhu J. Pore structure analysis and properties evaluations of fly ash-based geopolymer foams by chemical foaming method. Ceramics International, 2018, 44(16): 19989−19997
9. Heiken G, Vaniman D, French B M. Lunar Sourcebook—A User's Guide to the Moon. Cambridge: Cambridge University Press, 1991, 753
10. Montes C, Broussard K, Gongre M, Simicevic N, Mejia J, Tham J, Allouche E, Davis G. Evaluation of lunar regolith geopolymer binder as a radioactive shielding material for space exploration applications. Advances in Space Research, 2015, 56(6): 1212−1221
11. Alexiadis A, Alberini F, Meyer M E. Geopolymers from lunar and Martian soil simulants. Advances in Space Research, 2017, 59(1): 490−495
12. Zhang C, Nerella V N, Krishna A, Wang S, Zhang Y, Mechtcherine V, Banthia N. Mix design concepts for 3D printable concrete: A review. Cement and Concrete Composites, 2021, 122: 104155
13. Pilehvar S, Arnhof M, Pamies R, Valentini L, Kjøniksen A L. Utilization of urea as an accessible superplasticizer on the moon for lunar geopolymer mixtures. Journal of Cleaner Production, 2020, 247: 119177
14. Cesaretti G, Dini E, de Kestelier X, Colla V, Pambaguian L. Building components for an outpost on the lunar soil by means of a novel 3D printing technology. Acta Astronautica, 2014, 93: 430−450
15. Chu S H, Li L G, Kwan A K H. Development of extrudable high strength fiber reinforced concrete incorporating nano calcium carbonate. Additive Manufacturing, 2021, 37: 101617
16. Panda B, Tan M J. Rheological behavior of high volume fly ash mixtures containing micro silica for digital construction application. Materials Letters, 2019, 237: 348−351
17. Liu C, Wang X, Chen Y, Zhang C, Ma L, Deng Z, Chen C, Zhang Y, Pan J, Banthia N. Influence of hydroxypropyl methylcellulose and silica fume on stability, rheological properties, and printability of 3D printing foam concrete. Cement and Concrete Composites, 2021, 122: 104158
18. Labonnote N, Rønnquist A, Manum B, Rüther P. Additive construction: State-of-the-art, challenges and opportunities. Automation in Construction, 2016, 72(3): 347−366
19. Guo X, Yang J, Xiong G. Influence of supplementary cementitious materials on rheological properties of 3D printed fly ash based geopolymer. Cement and Concrete Composites, 2020, 114: 103820
20. Panda B, Ruan S, Unluer C, Tan M J. Improving the 3D printability of high volume fly ash mixtures via the use of nano attapulgite clay. Composites. Part B, Engineering, 2019, 165: 75−83
21. Zhang Y, Zhang Y, She W, Yang L, Liu G, Yang Y. Rheological and harden properties of the high-thixotropy 3D printing concrete. Construction & Building Materials, 2019, 201: 278−285
22. Liu X, Li Q, Li J. Shrinkage and mechanical properties optimization of spray-based 3D printed concrete by PVA fiber. Materials Letters, 2022, 319: 132253
23. Hambach M, Volkmer D. Properties of 3D-printed fiber-reinforced Portland cement paste. Cement and Concrete Composites, 2017, 79: 62−70
24. Raza M H, Zhong R Y, Khan M. Recent advances and productivity analysis of 3D printed geopolymers. Additive Manufacturing, 2022, 52: 102685
25. Zhou S, Zhu X, Lu C, Li F. Synthesis and characterization of geopolymer from lunar regolith simulant based on natural volcanic scoria. Chinese Journal of Aeronautics, 2022, 35(1): 144−159
26. Zhou S, Lu C, Zhu X, Li F. Preparation and characterization of high-strength geopolymer based on BH-1 lunar soil simulant with low alkali content. Engineering, 2021, 7(11): 1631−1645
27. McKay D, Carter J, Boles W, Allen C, Allton J. JSC-1: A new lunar regolith simulant. In: Engineering, Construction, and Operations in Space IV. Albuquerque, NM: American Society of Civil Engineer, 1994, 857–866
28. Zheng Y, Wang S, Ouyang Z, Zou Y, Liu J, Li C, Li X, Feng J. CAS-1 lunar soil simulant. Advances in Space Research, 2009,

43(3): 448−454
29. Robens E, Dbrowski A, Mendyk E, Goworek J, Sobczak J. Investigation of surface properties of lunar regolith—Part IV, annales UMCS. Chemistry, 2008, 63: 144−168
30. Ma G, Li Z, Wang L. Printable properties of cementitious material containing copper tailings for extrusion based 3D printing. Construction & Building Materials, 2018, 162: 613−627
31. Ranjbar N, Mehrali M, Kuenzel C, Gundlach C, Pedersen D B, Dolatshahi-Pirouz A, Spangenberg J. Rheological characterization of 3D printable geopolymers. Cement and Concrete Research, 2021, 147: 106498
32. Ivaniuk E, Friedrich Eichenauer M, Tošić Z, Müller S, Lordick D, Mechtcherine V. 3D printing and assembling of frame modules using printable strain-hardening cement-based composites (SHCC). Materials & Design, 2022, 219: 110757
33. ASTM D2196-20. Standard Test Methods for Rheological Properties of Non-Newtonian Materials by Rotational Viscometer. West Conshohocken, PA: ASTM, 2020
34. Sun C, Xiang J, Xu M, He Y, Tong Z, Cui X. 3D extrusion free forming of geopolymer composites: Materials modification and processing optimization. Journal of Cleaner Production, 2020, 258: 120986
35. Zhou S, Yang Z, Zhang R, Zhu X, Li F. Preparation and evaluation of geopolymer based on BH-2 lunar regolith simulant under lunar surface temperature and vacuum condition. Acta Astronautica, 2021, 189: 90−98
36. GB/T 17671-2021. Test Method of Cement Mortar Strength (ISO method). Beijing: Standardization Administration of the People's Republic of China, 2021 (in Chinese)
37. Ma G, Li Z, Wang L, Wang F, Sanjayan J. Mechanical anisotropy of aligned fiber reinforced composite for extrusion-based 3D printing. Construction & Building Materials, 2019, 202: 770−783
38. Ye J, Cui C, Yu J, Yu K, Xiao J. Fresh and anisotropic-mechanical properties of 3D printable ultra-high ductile concrete with crumb rubber. Composites. Part B, Engineering, 2021, 211: 108639
39. Petrie C J S. The rheology of fibre suspensions. Journal of Non-Newtonian Fluid Mechanics, 1999, 87(2): 369−402
40. Chen M, Liu B, Li L, Cao L, Huang Y, Wang S, Zhao P, Lu L, Cheng X. Rheological parameters, thixotropy and creep of 3D-printed calcium sulfoaluminate cement composites modified by bentonite. Composites. Part B, Engineering, 2020, 186: 107821
41. Chen M, Li L, Wang J, Huang Y, Wang S, Zhao P, Lu L, Cheng X. Rheological parameters and building time of 3D printing sulphoaluminate cement paste modified by retarder and diatomite. Construction & Building Materials, 2020, 234: 117391
42. Long W J, Lin C, Tao J L, Ye T H, Fang Y. Printability and particle packing of 3D-printable limestone calcined clay cement composites. Construction & Building Materials, 2021, 282: 122647
43. Ye J, Cui C, Yu J, Yu K, Dong F. Effect of polyethylene fiber content on workability and mechanical-anisotropic properties of 3D printed ultra-high ductile concrete. Construction & Building Materials, 2021, 281: 122586